Supplementary Information – Methods:

Numerical Model

Initial and Boundary Conditions. Initial conditions in most runs consist of a bare-bedrock plane 400 m wide by 2000 m long (extending from local base level to ridge crest), inclined at ~22°, seeded with white-noise elevation perturbations on the order of 1 m. In the run shown in Fig. 1 (main text), these perturbations are superposed upon a distribution of bedrock hillocks with a range of wavelengths and amplitudes. At the lower boundary, we use both open (fixed sediment elevation) and closed basin (no flux) conditions. Sediment flux does not occur across the upper boundary. Lateral boundary conditions are periodic and permit fluxes of runoff and sediment.

Rainfall, infiltration, and runoff. We calculate runoff based on rainfall intensity and duration, and infiltration. We select effective storm intensities, i ($m \cdot h^{-1}$), durations, t ($h \cdot storm^{-1}$), and number of storms per year, n, using hourly precipitation records for stations in the Mojave Desert, California (Baker, Iron Mountain, Mojave, Needles, Victorville) and Bakersfield, California (NOAA, 1999). We calculate infiltration depths explicitly at the time scale of individual storms by using a rearrangement of the Green-Ampt equation (Bedient and Huber, 1992), which predicts the depth of infiltration reached prior to surface saturation: $F = -\psi_f(\theta_s-\theta_u)/(1-i/K_s)$, where F is the infiltration depth that occurs implicitly over the course of a storm (m), ψ_f is the wetting front soil suction head (m), θ_s is the effective (saturated) sediment porosity, θ_u is the initial (unsaturated) moisture content, and K_s is the (saturated) hydraulic conductivity ($m \cdot h^{-1}$) of the sediment. Infiltrated water is assumed to ultimately evaporate, consistent with the absence of perennial streams in the desert environments considered here. Parameter values are based on sand-sized particles (Bedient and Huber, 1992): ψ_f = -0.05 m, θ_s = 0.4, θ_u = 0, and K_s = 0.03 $m \cdot h^{-1}$. When $i \leq K_s$, rainfall infiltrates until the regolith column's porosity is exceeded or until the rainfall is completely absorbed. When $i > K_s$, we compare the calculated infiltration depth, F, and the available pore space in the regolith column ($h \cdot \theta_s$), which is limited by local regolith thickness. If the pore space presents no limit to the calculated infiltration depth, F infiltrates. Otherwise, a volume infiltrates per unit area that is equal to the available pore space, with the remaining water, if any, contributing to runoff. Runoff out of each cell for both scenarios ($i \leq K_s$ and $i > K_s$) is then: $q_w = it\delta x - \min(F\delta x, h\theta_s\delta x) + q_n$, where q_w is the volumetric runoff per unit width per storm ($m^2 \cdot storm^{-1}$), q_n is the volumetric runoff per unit width per storm arriving in the cell from upstream neighbors ($m^2 \cdot storm^{-1}$), and δx is the cell size (m). On bare bedrock there is no infiltration. Hydraulic routing is performed according to the D∞ algorithm of Tarboton (Tarboton, 1997).

Topographic diffusion. Across each nearest-neighbor cell boundary, diffusive transport moves sediment downslope (Fernandes and Dietrich, 1997): $q_{s,d} = k_3 S$, where $q_{s,d}$ is the volumetric sediment flux per unit width ($m^2 \cdot y^{-1}$), S is slope between the centers of adjacent cells, and k_3 is the diffusivity ($1 \cdot 10^{-3}$ $m^2 \cdot y^{-1}$) (Hanks et al., 1984).

Sediment transport. Cells are sorted by elevation and are subjected, in order of descending elevation, to sediment transport processes. We multiply the sediment fluxes for each storm type by the number of storms of that type per year (n) and by the time step (10 years). Here $n = 4$, $i = 0.10$ m·h^{-1}, and $t = 1.0$ h·storm^{-1}, modeling the infrequent but geomorphically effective storms occurring in these environments on an annual basis. Sediment surface elevations are adjusted according to the difference of diffusive and advective fluxes in and out of each cell; bedrock elevations are decreased according to the weathering rule $W(h)$.

Supplementary Information – Figures:

We have performed 72 model simulations investigating the effects of varying the initial conditions and domain characteristics (initial regolith thickness, slope, distance from basin to crest, topographic perturbations, and boundary conditions), as well as process rates (transport efficiency (k_2), and weathering rates). In *all* experiments, the model produces pediments defined by an approximately smooth bedrock surface with a characteristically low slope (<0.2 or 11.3°), covered with a spatially homogeneous thickness of regolith (2-4 meters). Fig. DR1 shows this "pediment attractor", or attracting morphologic set to which the system consistently evolves, plotted within a "state-space" defined by regolith thickness and slope. The classic "pediment association" represents a highly ordered morphology; the spatially uniform pediments abut steeper, bare-bedrock slopes at localized piedmont junctions. Although less inevitable than a pediment alone, this association evolves in the model from *all* initial hillslope geometries in "open-basin" simulations (i.e., with a fixed alluvial elevation at the downslope boundary, simulating a bounding stream; see Fig. 3 in main text), using bedrock weathering rates appropriate for semiarid and arid granitic environments (Granger et al., 1996) (scaled by a bare-bedrock rate of 14 m·Ma^{-1}). Even for simulations in which the bedrock weathering rates are an order of magnitude higher, potentially representing more humid environments (bare-bedrock rate = 140 m·Ma^{-1}), a pediment association develops in open-basin simulations if initial regolith thickness is sufficiently small (not shown in Fig. DR1).

We also show more explicitly in this Supplementary Information the results of a subset of these simulations: 1) those incorporating random perturbations of initial topography (Figs. DR2,3) and lithology (Figs. DR4-8); 2) a simulation using multiple localized storms combined with a highly nonlinear transport law (Fig. DR9). 3) a 2-stage simulation illustrating exhumation of bedrock floor of pediment bounded upslope by a bare-bedrock upland and downslope by a depositional basin (Fig. DR10), and 4) a simulation employing a finer spatial discretization along with temporal fluctuations in rainfall characteristics that produce relatively small-scale bedrock knobs, or 'tors' (Fig. DR11). Fig. DR12 shows model results represented by cartoons in Fig. 3 of main text.

These combined results show that the highly structured pediment association emerges from the interactions between weathering and sediment transport dynamics internal to the model system, without being forced by specific initial conditions or model rules.

References:

Bedient, P.B., and Huber, W.C., 1992, Hydrology and Floodplain Analysis: Reading, MA, Addison-Wesley Publishing Co., 692 p.

Fernandes, N.F., and Dietrich, W.E., 1997, Hillslope evolution by diffusive processes: the timescale of equilibrium adjustments: Water Resources Research, v. 33, p. 1307-1318.

Granger, D.E., Kirchner, J.W., and Finkel, R., 1996, Spatially averaged long-term erosion rates measured from in situ produced cosmogenic nuclides in alluvial sediment: Journal of Geology, v. 104, p. 249-257.

Hanks, T.C., Bucknam, R.C., Lajoie, K.R., and Wallace, R.E., 1984, Modification of wave-cut and fault-controlled landforms: Journal of Geophysical Research, v. 89, p. 5771-5790.

NOAA, 1999, Hourly Precipitation Data, National Oceanic and Atmospheric Administration, National Climatic Data Center, Ashville, NC.

Tarboton, D.G., 1997, A new method for the determination of flow directions and upslope areas in grid digital elevation models: Water Resources Research, v. 33, p. 309-319.

DR1A

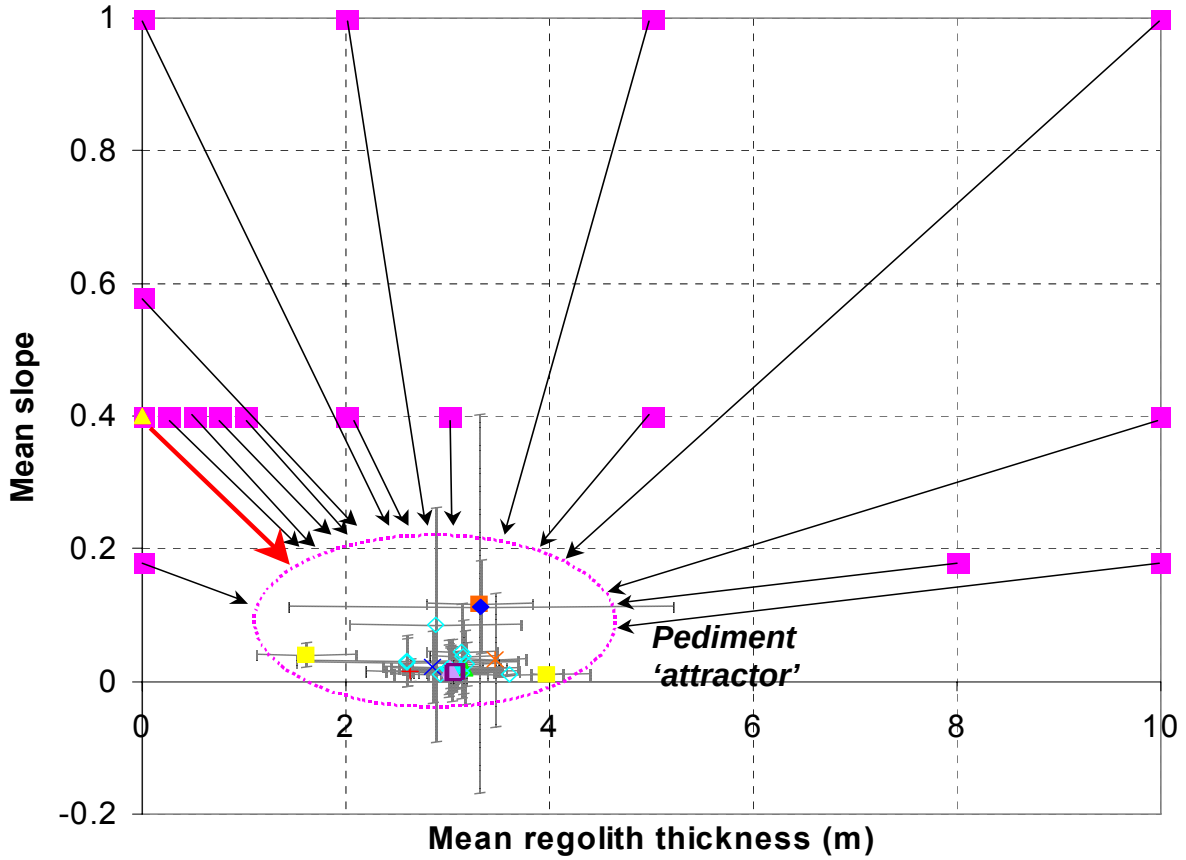
1
0.8
0.6
0.4
0.2
0
-0.2
0
2
4
6
8
10
Mean slope
Mean regolith thickness (m)
Pediment
'attractor'

DR1B

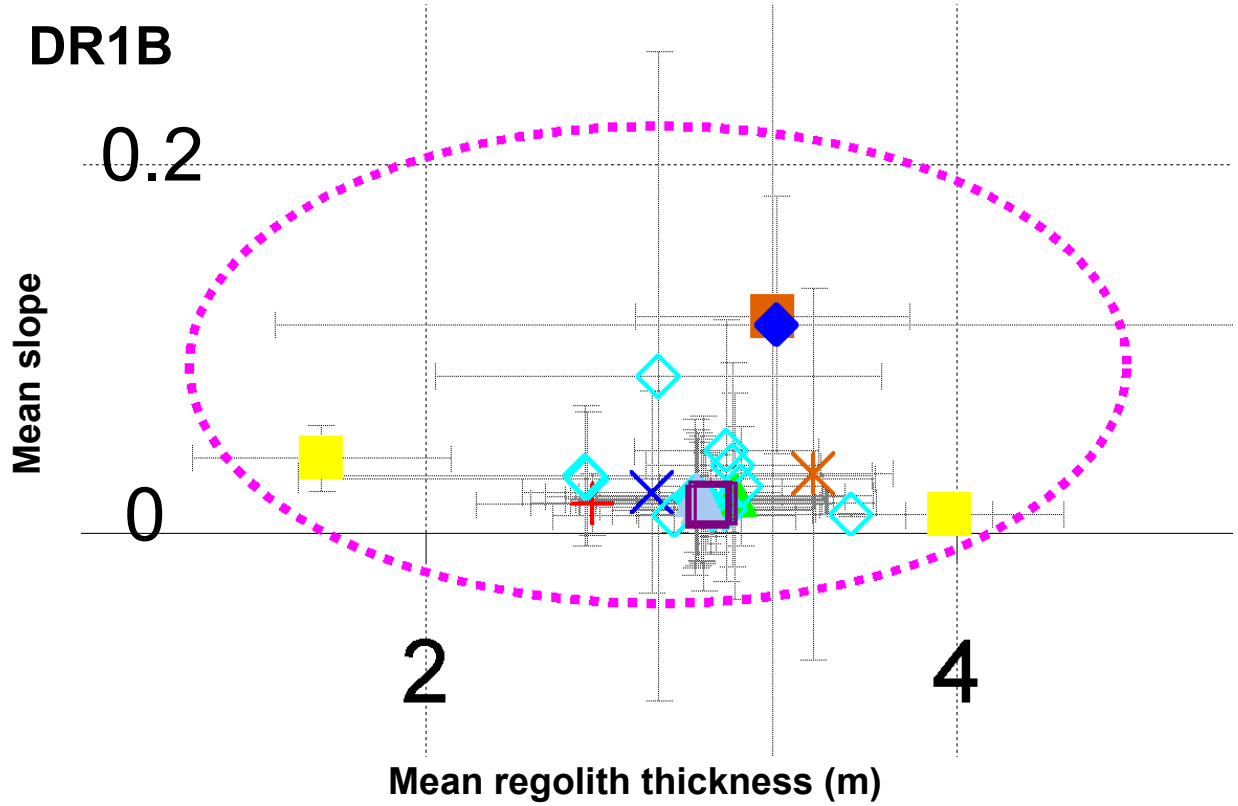
0.2
0
2
4
Mean slope
Mean regolith thickness (m)

Fig. DR1A,B. Initial conditions and evolved pediment morphology for 30 different simulations which use a bedrock weathering rate of ω_o-$k_1\omega_o$ = 14 m·Ma^{-1}. Points are plotted within a "state space" defined by the regolith thickness and slope. The pediment data are obtained from an algorithm that selects cells within each simulation that exhibit regolith thicknesses between 0.0001 and 6.0 m; 4-point nearest-neighbor gradients are calculated and averaged for these cells, and averages are also calculated for the regolith thicknesses. Horizontal and vertical error bars represent ± 1 standard deviation in pediment's regolith thickness and slope, respectively. Initial conditions are plotted as either those models that produce piedmont junctions (open-basin boundary conditions, magenta squares, ■) or those that do not (closed-basin boundary conditions, yellow triangles, ▲). The thick, red arrow represents multiple simulations that begin with slopes of 0.4 (22°) and zero regolith thickness and the black arrows represent all other simulations. Other symbols represent evolved pediments as follows: (■)simulation using a simple decaying exponential weathering rate-regolith thickness relationship; (▲)simulation using a modified sediment transport efficiency value (k_2 = 0.0007 or 0.003); (◊)simulations employing modified initial slope and/or regolith thickness (10-45°; 0-10 m); (□)randomly-placed 0-3 m elevation perturbations superimposed on an initially planar topography; (**X**)initial doubly-sinusoidal elevation perturbations superimposed on a planar topography (Fig. DR2); (▲)initial elliptic paraboloid elevation perturbations superimposed on a planar topography (Fig. DR3); (*)spatially-random perturbations of lithology (Fig. DR4); (■)weathering rates vary spatially by 3-fold (14 m·Ma^{-1} ≤ ω_o-$k_1\omega_o$ ≤ 42 m·Ma^{-1}) in a "checkerboard" pattern (Fig. DR5); (+)elliptic paraboloids defining elevation perturbations superimposed on an initially planar topography and variations in lithology (weathering rate) (Figs. DR6-8); (♦)highly nonlinear sediment transport (α = 2.0) combined with spatially-limited storm footprints with random sizes and locations (Fig. DR9).

Simulation Results and Sensitivity Analysis: Each figure shows initial (A) and developed (B) conditions. These figures represent an important sub-sample of the 72 simulations in our sensitivity analysis. All simulations shown here utilize "open-basin" boundary conditions, bedrock weathering rates scaled by ω_o-$k_1\omega_o$ = 14 m/Ma, and identical rainfall rates, unless otherwise noted. The remaining 65 simulations in our sensitivity analysis, many of which are used to construct the 'pediment attractor', are not shown because they exhibit behavior and morphology almost identical to that shown in Figure 3 of main text for open- and closed-basins, respectively.

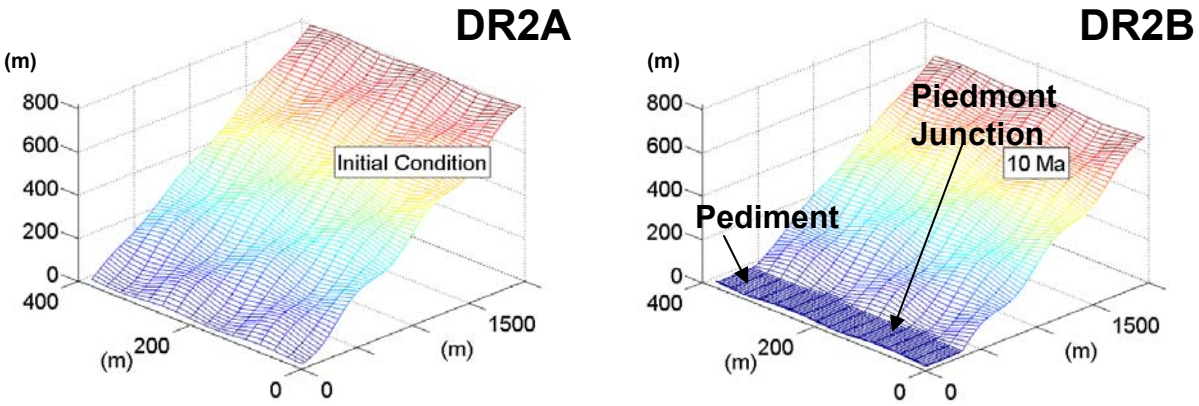

Fig. DR2A,B: Doubly-sinusoidal (amplitude 30 m, wavelength ~660 m) bedrock and alluvial elevation perturbations superimposed on an initially planar surface.

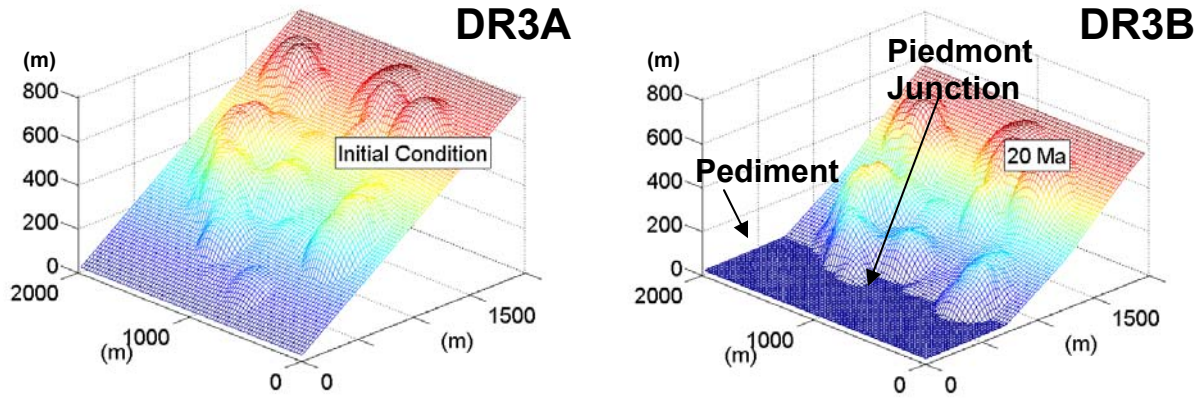

Fig. DR3A,B: Elliptic paraboloid elevation perturbations superimposed on an initially planar surface.

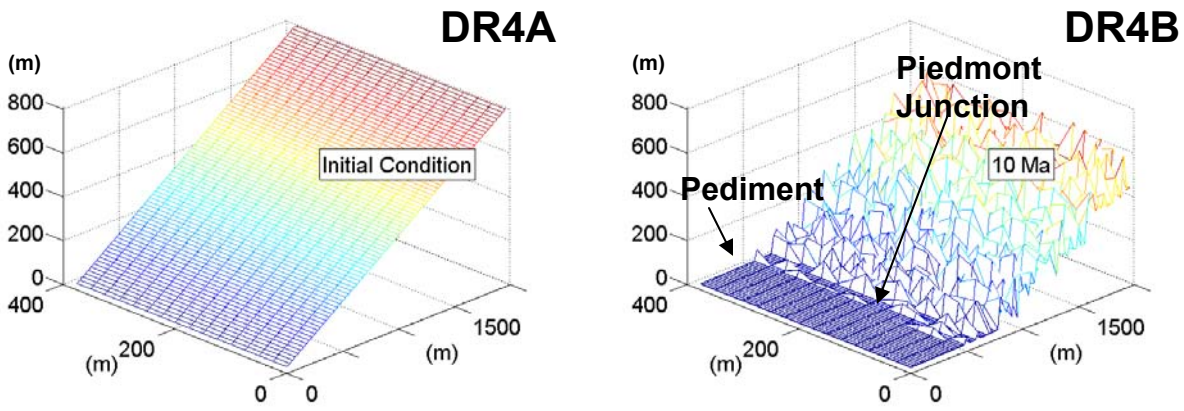

Fig. DR4A,B: Spatially-random perturbations of lithology (weathering rates varying up to 3-fold; 14 m/Ma ≤ ω_o-$k_1\omega_o$ ≤ 42 m/Ma). Note that although tors are produced here and in Fig. DR5 near the piedmont junction due to differential weathering (differing lithology producing spatial variations in weathering rates), our model produces tors when the lithology is spatially uniform (see Fig. DR11) as a result of the interactions between sediment transport and bedrock weathering dynamics (described in main text).

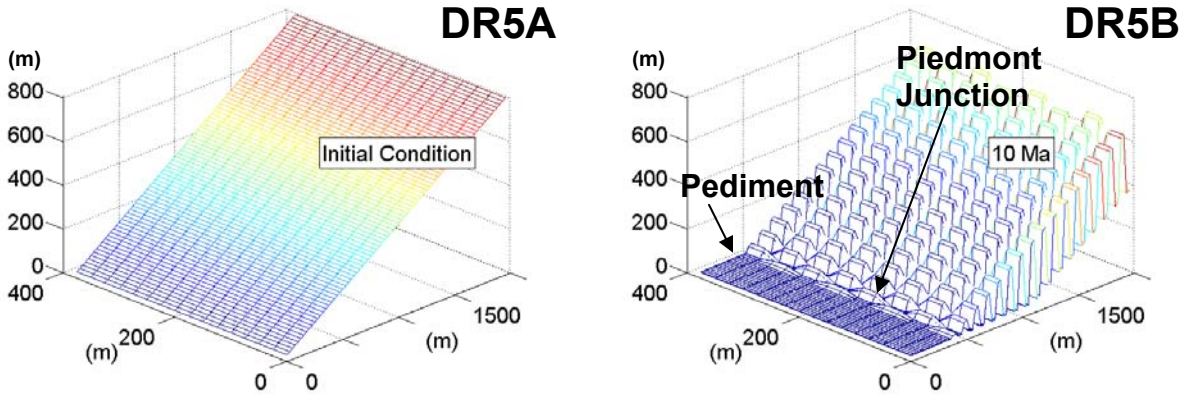

Fig. DR5A,B: Weathering pattern in which weathering rates vary spatially by 3-fold (14 m/Ma ≤ ω_o-$k_1\omega_o$ ≤ 42 m/Ma) in a "checkerboard" pattern.

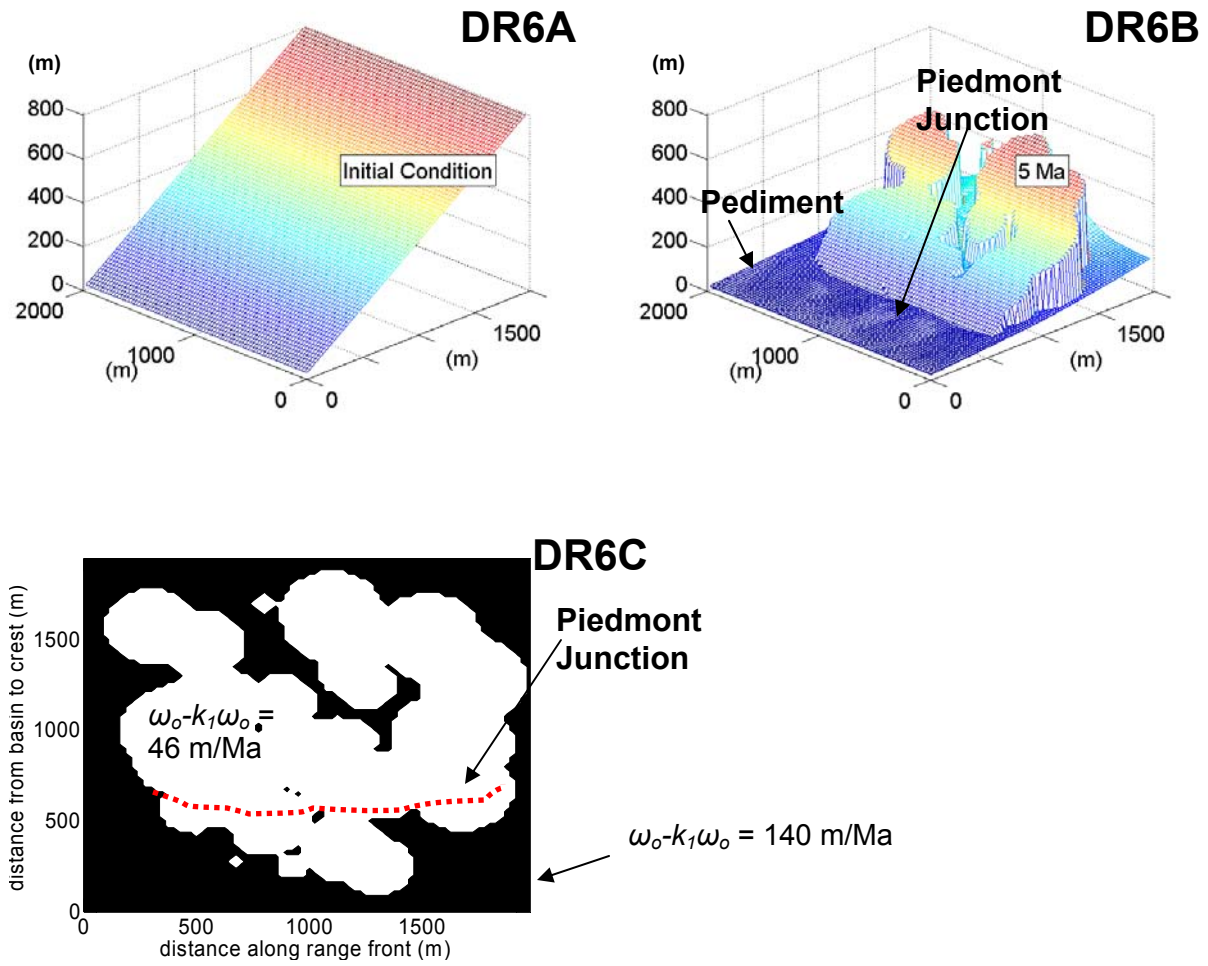

Fig. DR6A,B,C: Elliptic paraboloids correspond to more resistant rock, with panel **(C)** illustrating weathering-rate variation patterns and developing piedmont junction's (red dotted line) lack of weathering-rate sensitivity.

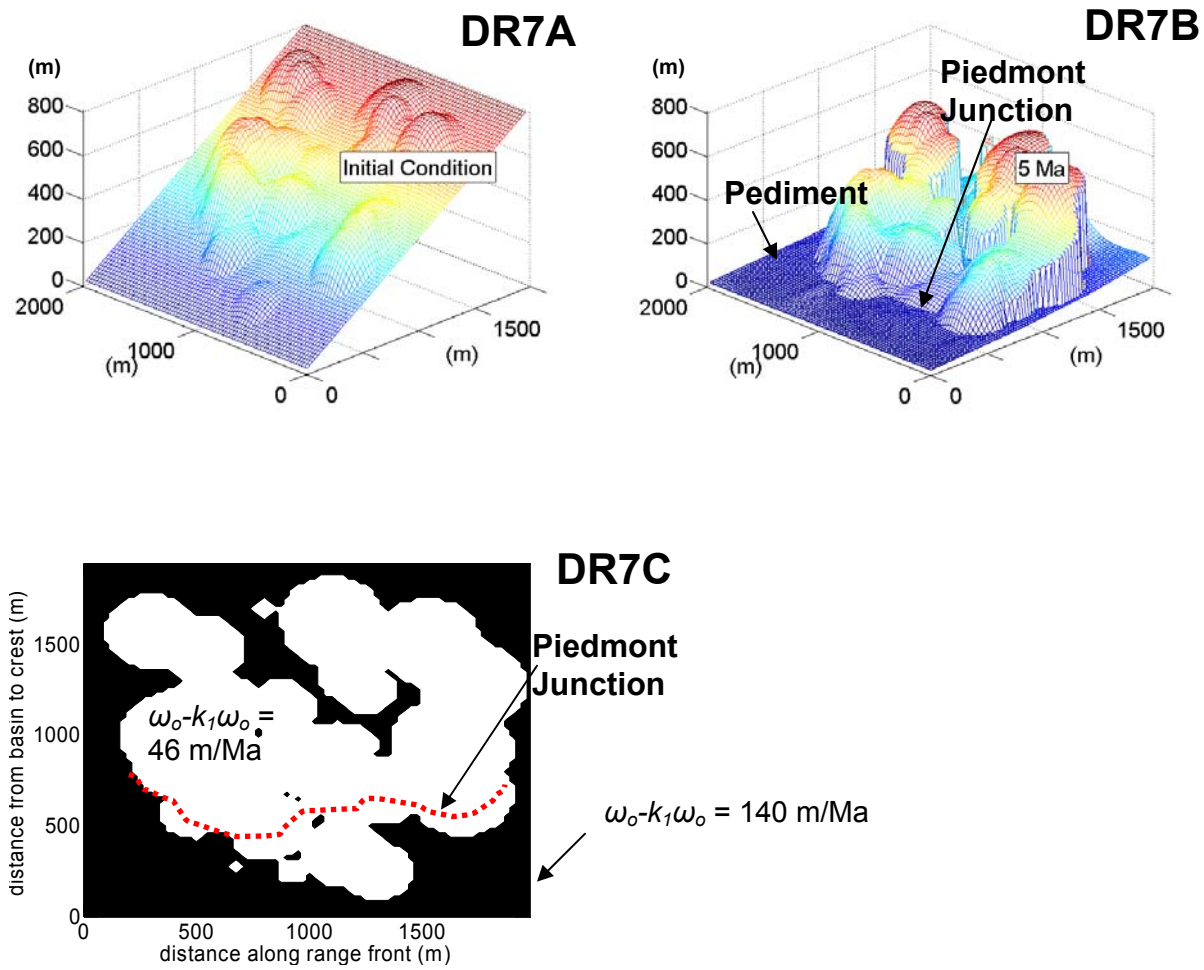

Fig. DR7A,B,C: Elliptic paraboloids correspond to initially elevated domains and more resistant rock, with panel **(C)** illustrating weathering-rate variation patterns and developing piedmont junction's (red dotted line) lack of weathering-rate sensitivity.

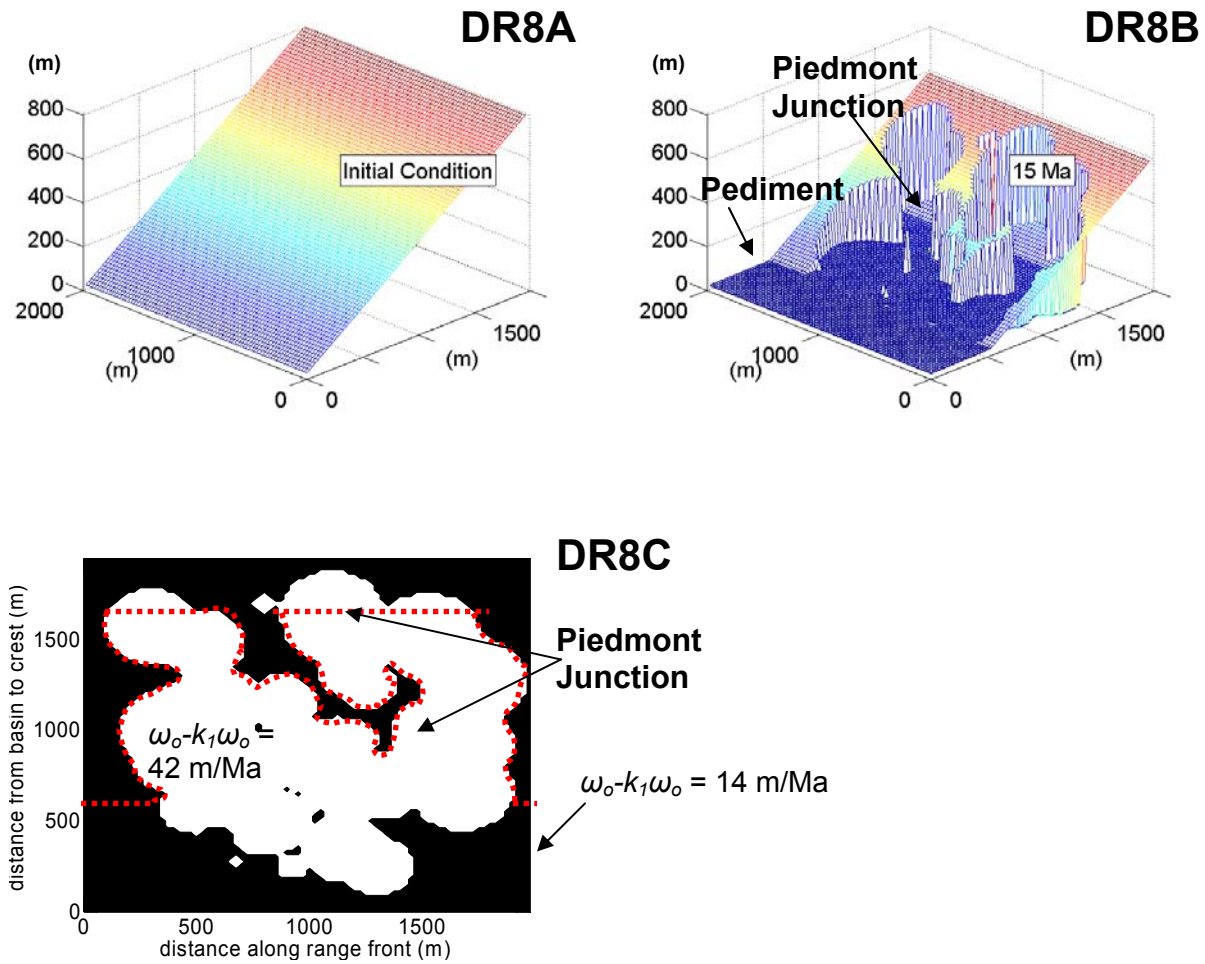

Fig. DR8A,B,C: Elliptic paraboloids correspond to initially less resistant rock, with panel **(C)** illustrating weathering-rate variation patterns and developing piedmont junction's (red dotted line) lack of weathering-rate sensitivity.

DR9

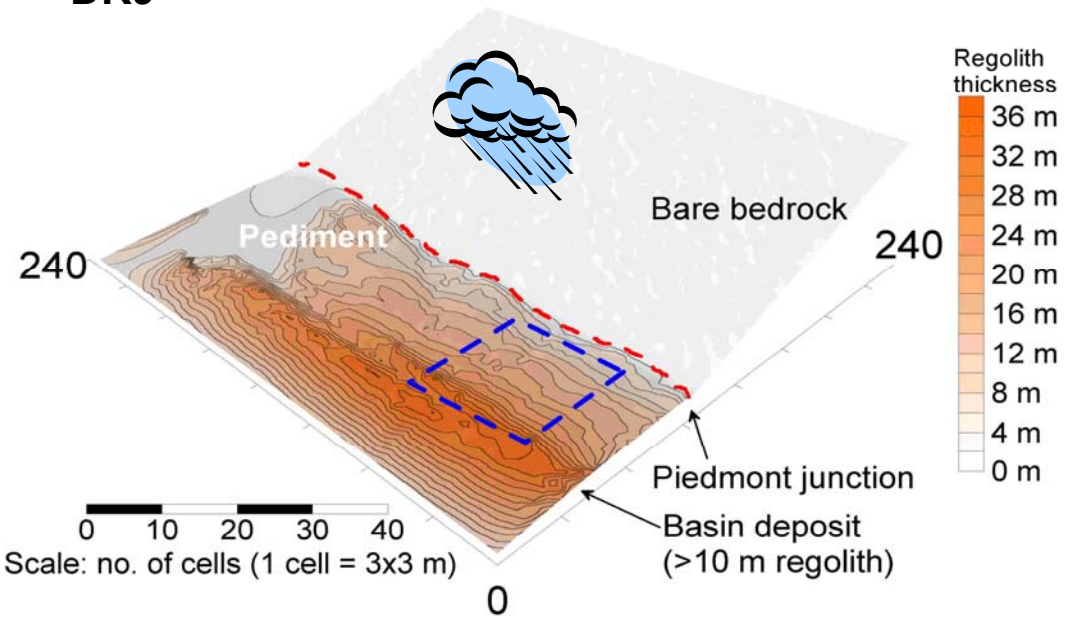

Fig. DR9: Contour plot of regolith thickness draped over topography for a model simulation using multiple localized storms combined with a highly nonlinear transport law ($\alpha = 2.0$). Basin deposits exhibit >10 m regolith thickness, while mountain mass above piedmont junction (dashed red line) is bare bedrock. The dashed blue box outlines a hypothetical, limited-footprint storm; storm footprint sizes and locations vary in time and space. Initial condition is an inclined (22°) bare-bedrock plane seeded with white noise elevation perturbations on the order of 1 m. The lower boundary is hydrologically-open (fixed alluvial elevation); sediment flux does not occur across the upper boundary; lateral boundary conditions are periodic and permit fluxes of runoff and sediment.

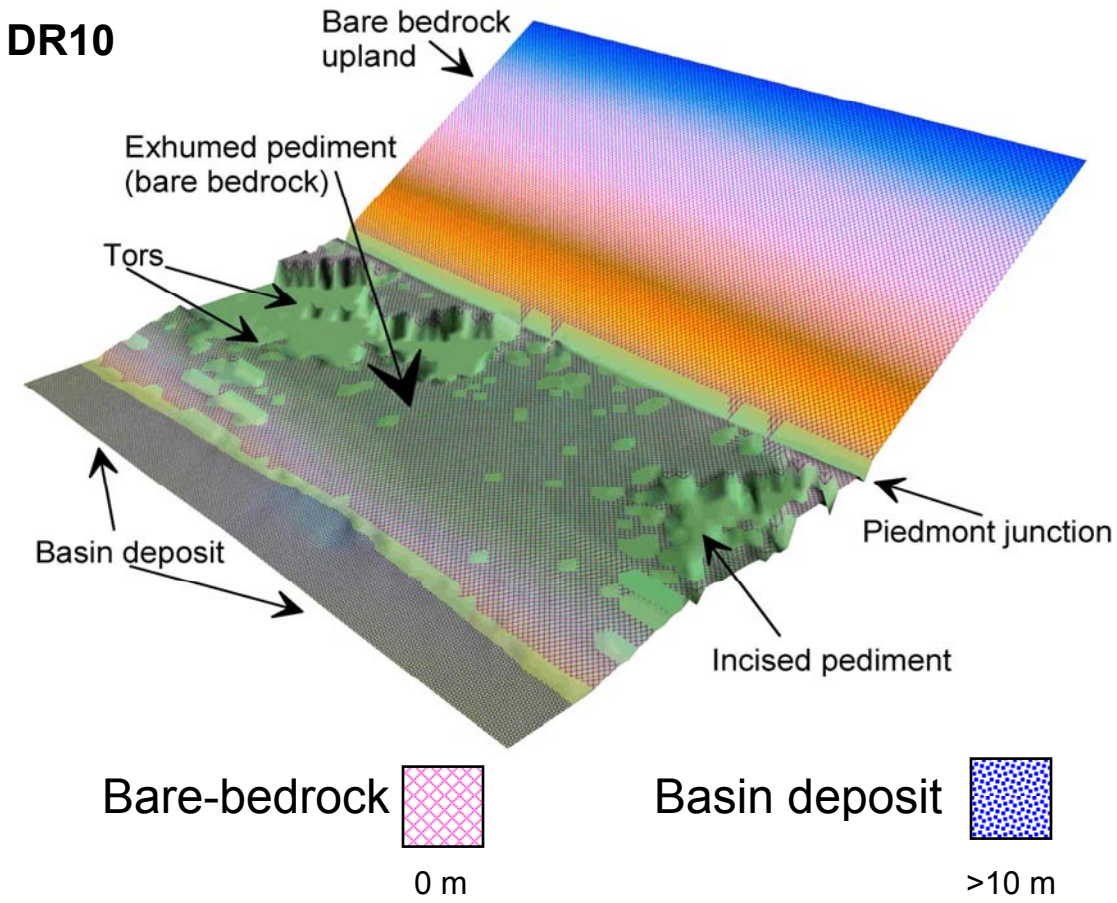

Fig. DR10: Output of 2-stage simulation illustrating exhumation of bedrock floor of pediment bounded upslope by a bare-bedrock upland and downslope by a depositional basin. Closed-basin (no flux) boundary conditions in the first stage (0-10 Ma) develop basin deposit, followed by base level incision (1 mm·y^{-1}) and increased rainfall (6 storms·y^{-1}) during the second stage (10-20 Ma). Initial condition is a flat, inclined (22°) bedrock plane mantled with 1 m of regolith and seeded with white noise elevation perturbations on the order of 1 m.

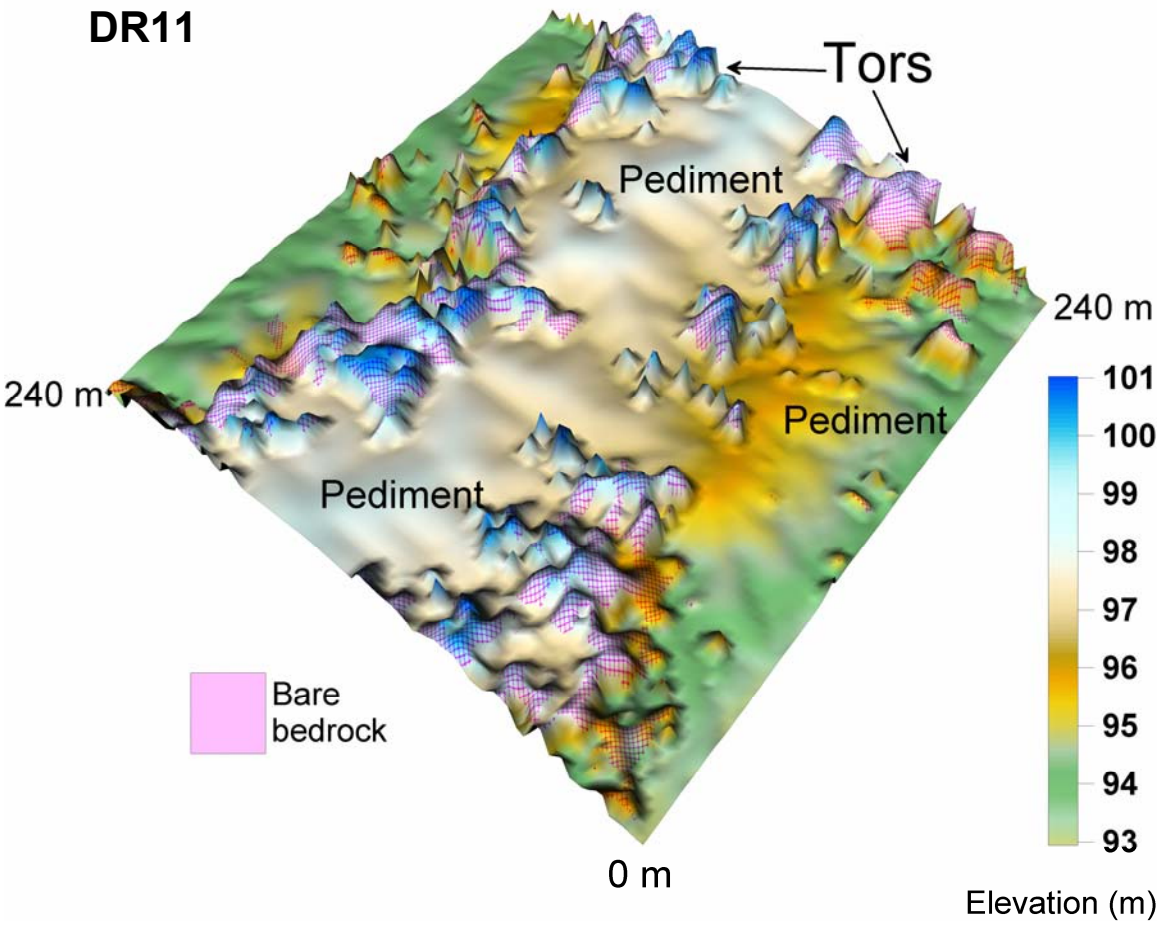

Fig. DR11: Output of simulation employing a finer spatial discretization (cell size = 3 m) along with temporal fluctuations in rainfall characteristics that produce relatively small-scale bedrock knobs, or 'tors' punctuating a smooth pediment. Lithological heterogeneities are not necessary for tor formation. A more thorough presentation of this aspect of the modeling is in preparation.

DR12a

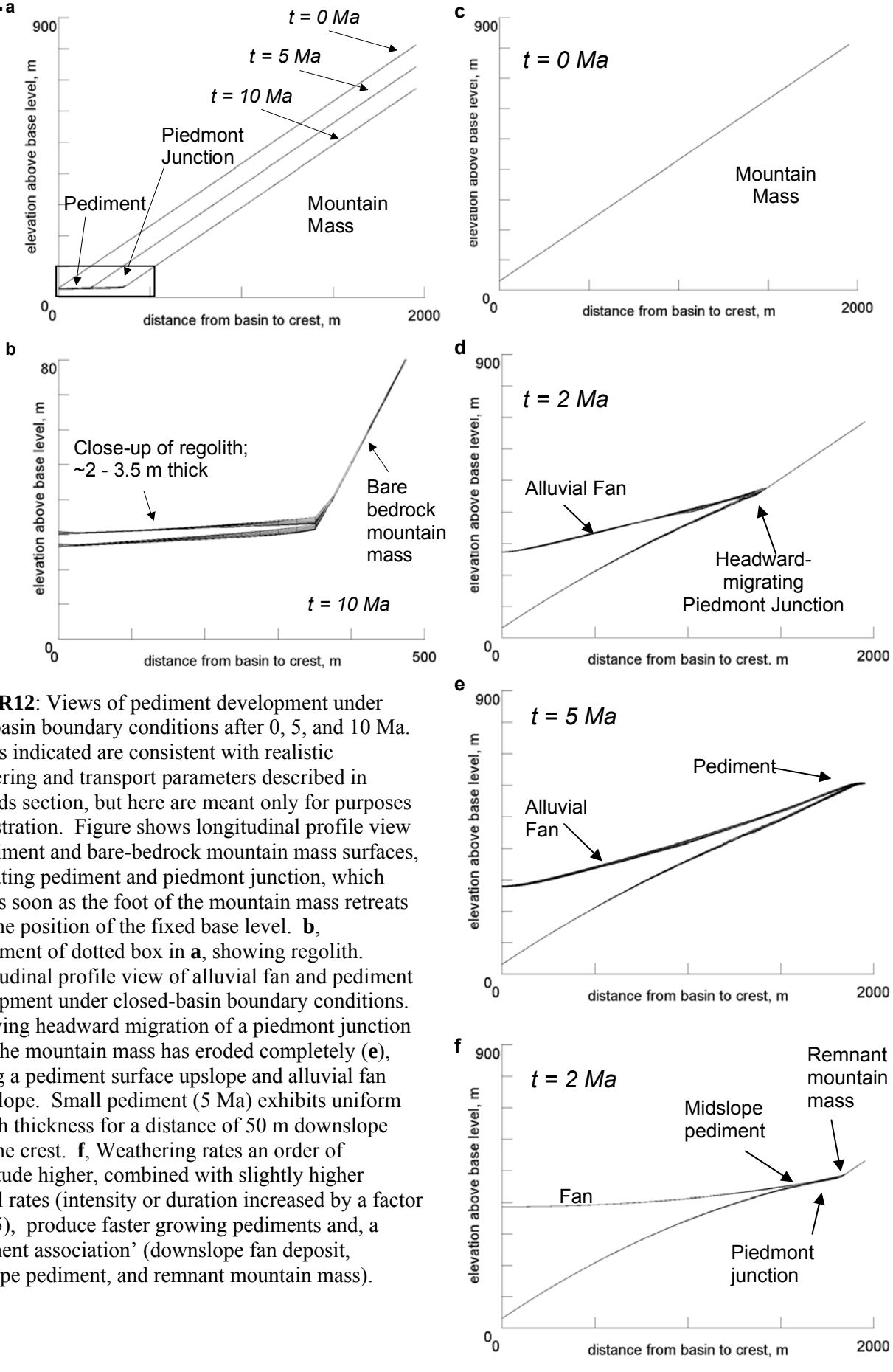

Fig. DR12: Views of pediment development under open-basin boundary conditions after 0, 5, and 10 Ma. **a**, Ages indicated are consistent with realistic weathering and transport parameters described in Methods section, but here are meant only for purposes of illustration. Figure shows longitudinal profile view of pediment and bare-bedrock mountain mass surfaces, illustrating pediment and piedmont junction, which form as soon as the foot of the mountain mass retreats from the position of the fixed base level. **b**, Enlargment of dotted box in **a**, showing regolith. Longitudinal profile view of alluvial fan and pediment development under closed-basin boundary conditions. Following headward migration of a piedmont junction (**c**,**d**), the mountain mass has eroded completely (**e**), leaving a pediment surface upslope and alluvial fan downslope. Small pediment (5 Ma) exhibits uniform regolith thickness for a distance of 50 m downslope from the crest. **f**, Weathering rates an order of magnitude higher, combined with slightly higher rainfall rates (intensity or duration increased by a factor of ~2.5), produce faster growing pediments and, a 'pediment association' (downslope fan deposit, midslope pediment, and remnant mountain mass).